Uniaxial and biaxial strain engineering in 2D MoS₂ with lithographically patterned thin film stressors

Cite as: Appl. Phys. Lett. 118, 213104 (2021); doi: 10.1063/5.0049446 Submitted: 4 March 2021 · Accepted: 10 May 2021 · Published Online: 26 May 2021







Ahmad Azizimanesh, 🐚 Tara Peña, 🐚 Arfan Sewaket, Wenhui Hou, 🐚 and Stephen M. Wu^{1,2,a} 🕞



AFFILIATIONS

ABSTRACT

We introduce a controllable approach to selectively strain (uniaxially or biaxially) MoS2 by depositing e-beam evaporated thin film stressors with a lithographically patterned stripe geometry. This type of strain engineering has been highly successful in commercial silicon-based CMOS processes to enhance carrier mobility by applying uniaxial strain in MOSFET channels. We attempt to outline the basis for using the same techniques with 2D van der Waals materials with weak out-of-plane bonding. The stressor in this work is chosen to be optically transparent to examine the strain distribution within MoS₂ using Raman spectroscopic mapping. MoS₂ flakes with partial tensile stressor coverage show large tensile strains close to free edges and compressive strain at the center of the stressor strip. Both in-plane and out-of-plane strains are observed. By varying strip width and MoS₂ flake thickness, the geometric distribution of both tensile and compressive strained regions can be controlled. The directionality of strain induced by the stressor strip is also explored through polarized Raman spectroscopy where MoS₂ shows 0.85% uniaxial strains occurring at strip edges for 25 N/m film force and biaxial strains occurring at strip centers using the same stressor. Using these combined techniques, we show that strain in 2D materials can be uniquely engineered by design to selectively exhibit tension/compression, uniaxiality/biaxiality, and directionality relative to crystal axes through simple lithographic patterning of stressed thin films. This opens the opportunity to create strain patterned devices with a wide variety of strain-tunable 2D materials properties (electronic, optical, superconducting, etc.), now controllable by micro/nanolithographic design.

Published under an exclusive license by AIP Publishing. https://doi.org/10.1063/5.0049446

Strain engineering has long been used by the semiconductor industry for strained silicon technology, 1-4 where it has been used since the 90 nm technology node to enhance electron or hole mobility. In this process, it is critical that within this single chip, the strain can be selectively controlled for magnitude, compression/tension, uniaxiality/biaxiality, and directionality relative to the silicon crystal axes for each transistor, since the strain parameters for mobility enhancement for each individual p-channel and n-channel MOSFET are not the

Currently, two-dimensional (2D) materials have been explored to create the next generation of integrated electronic or photonic circuits. Within this materials class, there are a wide variety of strainsensitive electrical, optical, mechanical, magnetic, superconducting, and topological properties available to control.^{5–14} Strain engineering in 2D materials has been limited to macroscale mechanical approaches such as bending flexible substrates, 15-17 engineered ripples, 18 substrate thermal expansion, ¹⁹ diamond anvil cells, ²⁰ and suspended membrane structures²¹ in previous works. While these methods work on a global

scale, they are not directly translatable to devices that exist on-chip in a densely integrated system. Recently, progress has been made on microscale and nanoscale strain engineering methods to locally strain 2D materials^{22–27} but a technique with as much simultaneous control over all strain parameters as CMOS strain engineering has not yet appeared.

Recently, our group proposed a technique to strain exfoliated 2D materials using evaporated thin film stressors similar to CMOS strain engineering techniques that have been used in the past. Using a single evaporation step, a stressed thin film was deposited over the entire exfoliated MoS₂ flake. Raman spectroscopy revealed uniform in-plane tensile or compressive strains throughout the whole flake.²⁸ These approaches allow for controllable strain magnitude, which was shown to be directly proportional to film force (film stress \times film thickness), with controllable strain type (tensile or compressive). But since stressors were deposited over the entire flake, there was no geometric control of the strain distribution within each flake. Local and directional strain patterning was a critical ingredient for device-by-device strain

Department of Electrical and Computer Engineering, University of Rochester, Rochester, New York 14627, USA

²Department of Physics and Astronomy, University of Rochester, Rochester, New York 14627, USA

a)Author to whom correspondence should be addressed: stephen.wu@rochester.edu

engineering in strained silicon MOSFETs and will also be a critical ingredient for any future micro/nanoscale control of strain in 2D devices.

In this work, using lithographically patterned thin film stressors, we may overcome any of the previously mentioned limitations. We will show that this technique can provide both types of strain (tensile and compressive) with a single stressor and that uniaxial or biaxial strain can be applied in a controlled direction along crystal axes by orienting the patterned stressor relative to the flake. Additionally, we can also apply out-of-plane strains to the 2D material on top of the typical in-plane strains mentioned in our previous works on this topic.

We strain a few-layered MoS_2 with transparent thin-film stressors with a strip geometry and use Raman spectroscopic mapping to study the strain distribution within MoS_2 flakes. We choose MoS_2 because it is extremely well-studied with respect to its Raman signature and how it is affected by strain, defects, and doping. ^{29–31} Raman signatures of 2D MoS_2 have two dominant peaks at $\sim 384~cm^{-1}~(E_{2g}^1)$ and $\sim 407~cm^{-1}~(A_{1g})$, which represent the in-plane and out-of-plane phonon modes, respectively. Initial results are measured with linearly polarized incident light, but the scattered light was collected with no analyzer (Figs. 1–3), later we measure polarization-dependent Raman in the parallel polarization setup where the incident light and the analyzer are along the same axis (Fig. 4).

To effectively strain 2D MoS₂ flakes, they need to be well-adhered to the substrate after mechanical exfoliation. Otherwise, in poorly adhered MoS₂ flakes, strain causes delamination of the flakes from the substrate. The thin film stressors in stripe geometries are deposited using e-beam evaporation and photolithographically patterned on the substrate with a liftoff technique. Nearly all evaporated materials build intrinsic stress during deposition which is a

characteristic of each material. ^{32,33} In order to be consistent with our previous work on uniformly straining 2D materials, we use the same thin-film stressor, ²⁸ chosen to be a trilayer of 10 nm Al₂O₃, 100 nm MgF₂, and 10 nm Al₂O₃. The bottom Al₂O₃ layer improves the adhesion of the MgF₂ stressor to the MoS₂, which is necessary for the strain to be transferred from the stressor to the 2D flakes. The MgF₂ layer is the stressor and the top Al₂O₃ is a protective layer for MgF₂ that prevents stress relaxation over time due to environmental interaction. ^{32,34} A total of tensile film stress and film force of 0.21 GPa and 25 N/m were measured in the deposited stressor, respectively. From our previous work, we know strain engineering works with the MgF₂ layer by itself also, albeit with a lower magnitude of strain. See the supplementary material for more detailed information on methods.

Figure 1(a) illustrates a three-layer MoS_2 flake capped with an $Al_2O_3/MgF_2/Al_2O_3$ stressor in a stripe geometry and shows the typical structure of devices in this work (stressor patterned perpendicular to flake). Figure 1(b) presents the E_{2g}^1 Raman peak frequency (in-plane phonon mode) map across the MoS_2 flake. Darker regions close to edges of the stressor show that E_{2g}^1 has shifted down in those regions meaning MoS_2 is under tensile strain at both edges. At the center of stressor, E_{2g}^1 has shifted up and it means MoS_2 is under compressive strain. The amount of E_{2g}^1 peak shift is proportional to amount of in-plane strain in MoS_2 . Tensile stressor thin films try to release the stress by contracting, 28,36 thus in stripe geometry stressors, the free edges of the stressor produces the so-called film-edge-induced stress which causes tensile strain to be transferred around free edges of the stressor. 37,38

Figure 1(c) illustrates the map of A_{1g} Raman peak frequency (out-of-plane phonon mode) of the same flake. The map shows that the A_{1g} peak has considerably shifted down at the edges. At the center,

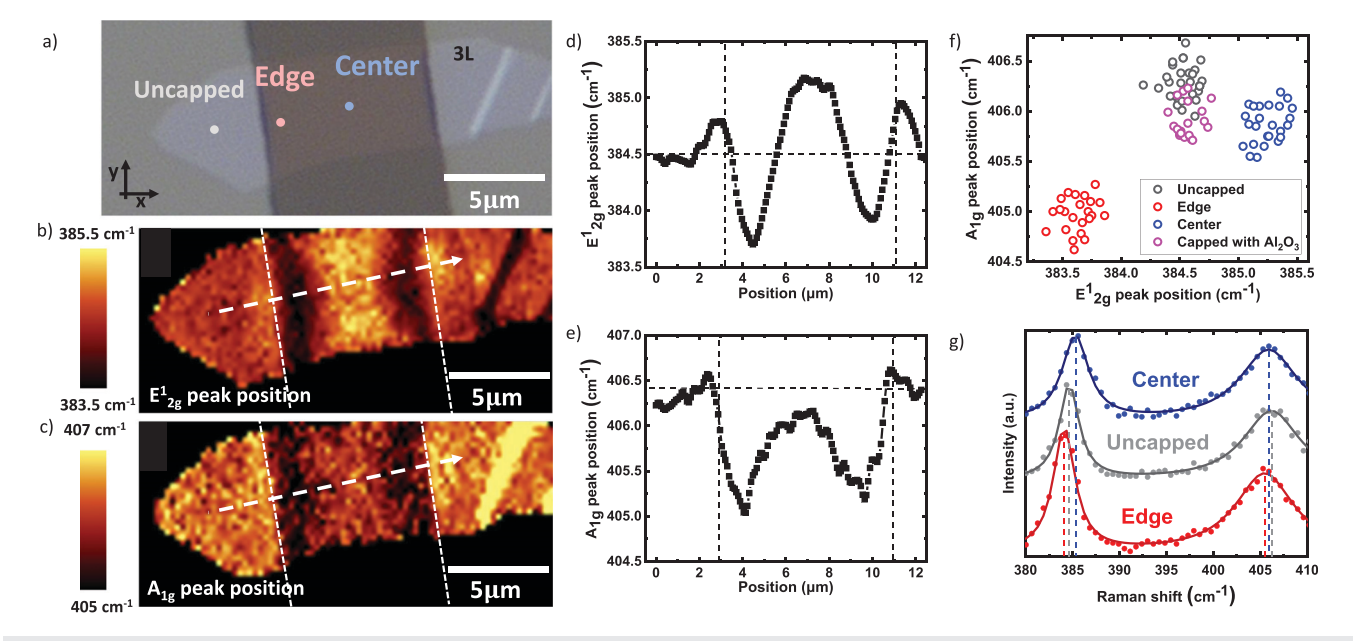


FIG. 1. (a) Optical image of a 3L-MoS₂ flake coated with patterned $A_2O_3/MgF_2/Al_2O_3$ stressor, incident light is polarized in y direction, the scattered light was collected with no analyzer. (b) and (c) E_{2g}^1 and A_{1g} Raman peak position map of the same MoS₂ sample. (d) and (e) E_{2g}^1 and A_{1g} Raman peak position profile along the arrows in E_{2g}^1 and A_{1g} maps, respectively. (f) A_{1g} Raman peak position as a function of E_{2g}^1 Raman peak position for locations in (a), along with a control Al_2O_3 coated sample. (g) Three representative Raman spectra from the MoS₂ sample in (a).

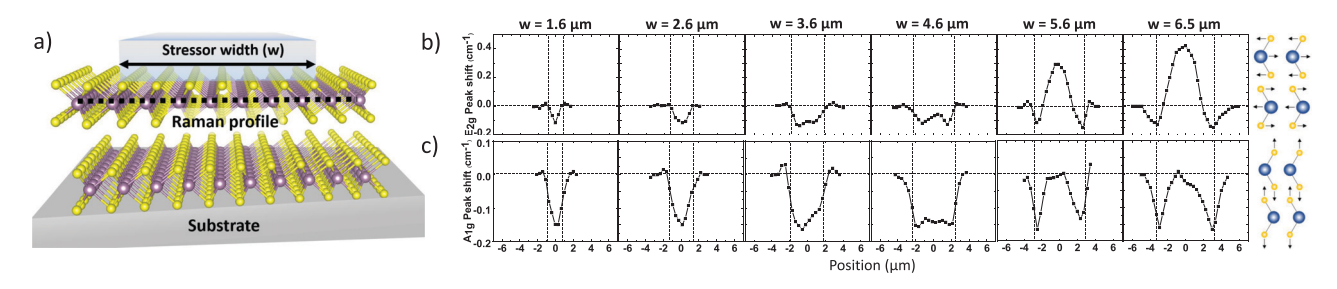


FIG. 2. (a) Raman profile across stressor width on MoS₂ (b) E¹_{2a} (top) and A_{1g} (bottom) peak shift profile relative to unstrained 8L MoS₂ for different stressor linewidths

there is no significant A_{1g} peak shift. This likely means that the MoS₂ flake is under tensile out-of-plane strain at the edges of the stressor. Linecuts of E_{1g}^1 and A_{1g} peak positions along the arrows on the corresponding Raman map are presented in Figs. 1(d) and 1(e), respectively.

Figure 1(f) presents the A_{1g} peak position as a function of E_{2g}^1 peak position of multiple Raman measurements of uncoated, Al_2O_3 coated 3L MoS_2 and different regions of the stressor from device in Fig. 1(a). Figure 1(g) presents the Raman signals from three spots on the flake. The doping/defects induced in MoS_2 from deposition of Al_2O_3 alone does not shift the E_{2g}^1 peak considerably while there are significant E_{2g}^1 peak shifts at the center and edges of the stressor.

In the $\rm \mathring{A}l_2O_3$ coated 3L MoS₂, the $\rm A_{1g}$ peak has shifted down slightly $\sim 0.4 \, \rm cm^{-1}$, which may be due to either a doping/damage effect from e-beam evaporation of $10 \, \rm nm \, Al_2O_3$ or dielectric encapsulation induced band bending. It indicates that any further shifts in $\rm A_{1g}$ peak

are coming from strain effect alone. The A_{1g} peak distribution at the edges of the Al₂O₃/MgF₂/Al₂O₃ stressor shows much larger peak shifts compared to the Al₂O₃ coated sample. The A_{1g} peak position at center of the stressor has similar down-shift to the Al₂O₃ coated sample, indicating no strain. Therefore, the A_{1g} peak shift at the edges of the stressor is likely due to out-of-plane strain and not doping/defects since the center is covered with the same stressor. We have also eliminated the possibility of photo-excited charge accumulation due to strain-induced bandgap variation at the edges, further discussion is presented in the supplementary material (Figs. S3-S6). All literature sources of strained trilayer MoS2 show the minimal movement of the A_{1g} peak with respect to in-plane strain alone, leading us to conclude that the A_{1g} peak shifts are not due to concomitant shifts from inplane strain effects alone. These combined arguments further strengthen the case that we are applying out-of-plane tensile strain at the stripe edges. Out-of-plane strain induced by stressor layers has

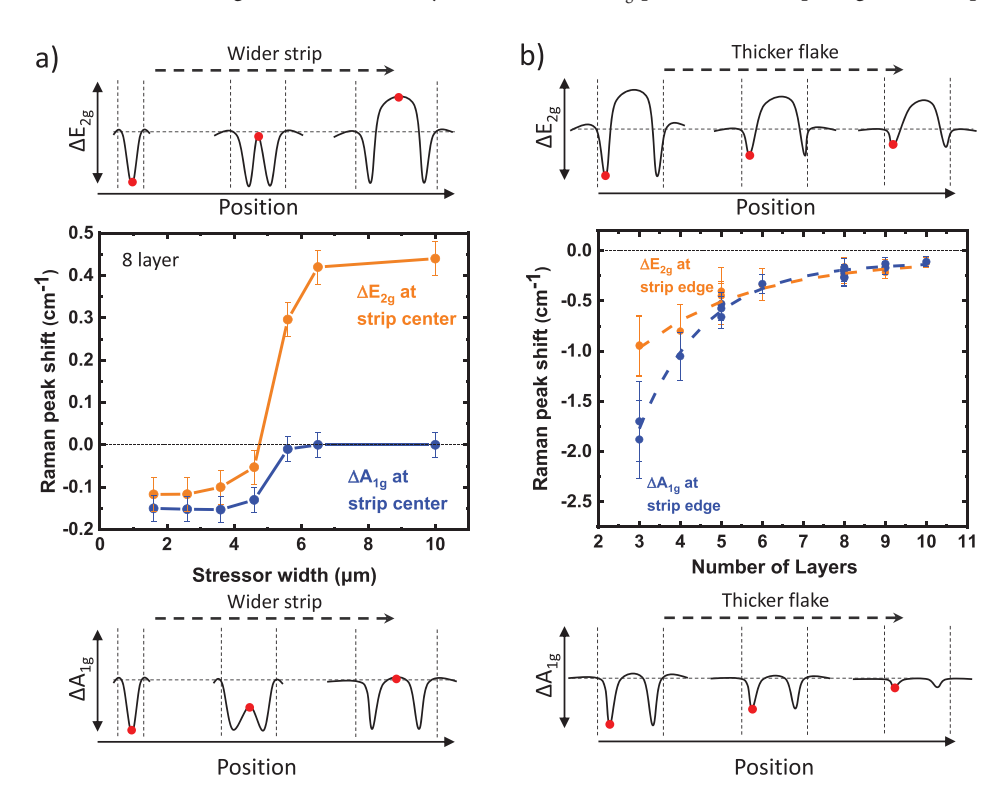


FIG. 3. (a) E_{2g}^1 and A_{1g} peak shifts in the center of the stressor in an 8L-MoS $_2$ flake as a function of the stressor width. (b) E_{2g}^1 and A_{1g} shifts at the edge of the stressor as a function of the flake thickness. Data include all stressor widths since edge strain is not a function of stressor width (specific stressor widths are presented in the supplementary material).

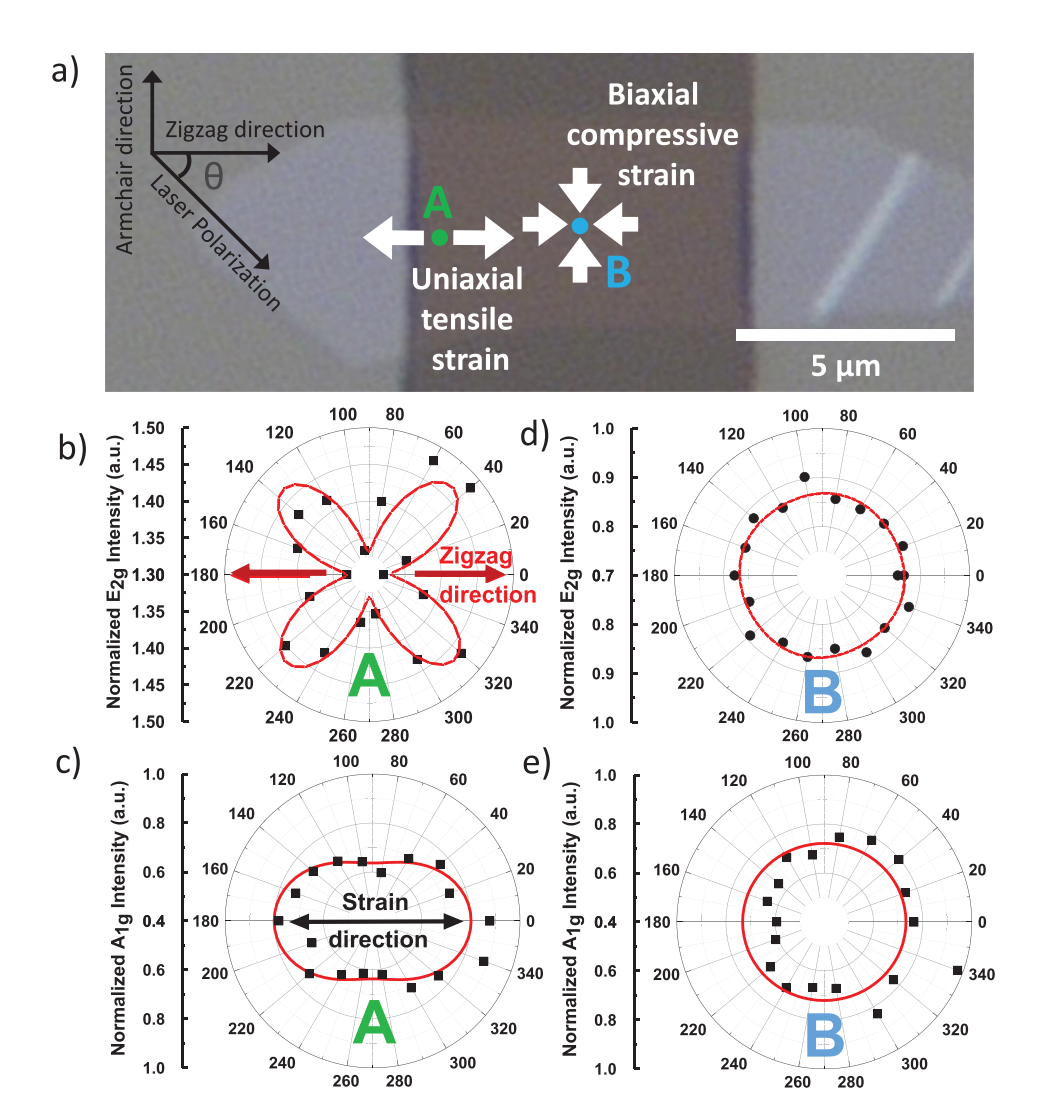


FIG. 4. (a) Strain directionality under the stressor strip, incident light is parallel to analyzer polarization. (b) and (c) Normalized amplitude of E_{2g}^1 and A_{1g} peaks as a function of the angle between the laser polarization direction and the zigzag direction of MoS $_2$ from point A. (d) and (e) The same results from point B.

been seen regularly in strain-engineered 3D-bonded silicon but has not been observed in weakly out-of-plane bonded 2D materials until here.³⁷

We have further investigated the effect of stressor width on strain distribution in an 8L MoS₂ sample and the results are presented in Fig. 2. As illustrated in Fig. 2(a), the Raman profile is collected across the width of the stressor. The stressor here is still the same $Al_2O_3/MgF_2/Al_2O_3$ thin film with the same amount of tensile stress.

Figure 2(b) presents the $\rm E_{2g}^1$ Raman peak shift distribution for different stressor widths. Raman peak shift at the stripe edges is due to strain induced by edge forces and exists regardless of stressor width. In wider stressors, a compressive region forms in the stressor center as the stressor width gets larger. Similar behavior has also been observed in the Raman study of variable width stressors on silicon substrates, where in-plane and out-of-plane relaxations of the narrowest stressors induce only one type of strain. In this proposed model, center strain evolves from compressive to tensile in silicon with increasingly narrow stressor stripes due to a redistribution of edge forces when edge regions meet, a behavior similar to our experimental results.

An important factor to consider is that the Raman laser spot size is approximately 0.7 μ m, and the strain distribution of the narrowest stressors cannot be precisely resolved within this limit. In Raman measurements of strain in silicon with narrow tensile stressors, it has been suggested that we cannot eliminate the possibility that a very narrow region of compressive strain might exist at the center that cannot be resolved by Raman.³⁹ If these regions do exist though, they are exceptionally narrow compared to the width of the stressor since there is almost no peak shift magnitude difference between the center of narrow stressors and edge regions of wide stressors.

The A_{1g} Raman peak shift across the stressor is presented in Fig. 2(c). Similar to the in-plane strain distribution the out-of-plane peak shifts are also subject to edge effects for all stressor widths. Only tensile out-of-plane strain exists within the narrowest stressors. As stressors get wider, the center region evolves into a region with no A_{1g} peak shift, suggesting there is no applied out-of-plane strain at the center of the wide stressors. Regardless of stressor width, tensile out-of-plane strain in the flake always happens at the edges meaning the out-of-plane strain is an edge-induced effect. For these results, we also

cannot eliminate the possibility of subdiffraction limited strain variation for the narrowest stressors, for the same reason as the in-plane strain distribution, but if they exist they are small since there is no peak shift magnitude change between the center of the narrowest stressors and the edge of the wider stressors.

Since the center of the stressor shows tensile to compressive strain evolution by varying stressor width, Fig. 3(a) presents the amount of $\rm E_{2g}^1$ and $\rm A_{1g}$ peak shift at the center of the stressor for an eight-layer $\rm MoS_2$ flake as a function of stressor width. The evolution in the strain at the center of stressors is due to the impact of in-plane and out-of-plane edge forces on the center region. Further increase in width of the stressor does not increase the amount of Raman peak shift at the center, which is the limit of compressive strain that is achievable with this specific stressor in the wide stressor limit.

Figure 3(b) shows the maximum E_{2g}^1 and A_{1g} peak shifts at the edge of the stressor as a function of the thickness of the flake. These values consistently show the same trend for all stressor widths and display an exponential decay in Raman peak shift magnitude as a function of flake thickness, hinting at a natural decay length scale. Our previous work on this topic showed that the maximum amount of strain is applied to the top layer which is in contact with the stressor, and strain in each individual layer below subsequently has less strain transferred into it.²⁸ We find the decay length scale for the in-plane phonon mode from Fig. 3(b) to be the same as our previous work; therefore, we adjust the biaxial E_{2g}^1 Raman peak shift (cm⁻¹) vs strain (%) value to a conservative uniaxial value from the literature and we estimate the edge strain magnitude to be 0.85% in the top layer of each flake. This matches our previous value of 0.85% biaxial strain in MoS₂ with nonpatterned stressors for 25 N/m film force (the same film force we used in this work). At the center of the stressor far from the free edges, decay is also observed with respect to flake thickness but depends on stressor width and stress redistribution inside the stressor layer (Fig. S2). A more detailed analysis on force redistribution inside the stressor is needed to estimate the center strain magnitude.

To understand strain direction produced by the proposed patterned stressors more clearly, we use polarization-dependent Raman spectroscopy at the edge and center of the stressor in our MoS_2 flake with stripe stressors to find strain directionality [Fig. 4(a)]. The Raman measurements that have been conducted for this experiment are in a parallel polarization setup where the incident laser beam and analyzer polarization are the same. Raman measurement is done at different angles by just rotating the sample alone in this configuration.

The amplitude of E_{2g}^1 and A_{1g} peaks of MoS₂ under a parallel polarized Raman setup are proportional to the following equations, respectively:⁴⁰

$$\mathrm{Amp}\Big(\mathrm{E}^1_{2\mathrm{g}}\Big) \propto \mathrm{asin}^2(2\theta + \varphi) + \mathrm{bcos}^2(2\theta + \varphi), \tag{1}$$

$$Amp(A_{1g}) \propto \left(csin^2(\theta - \varphi) + dcos^2(\theta - \varphi)\right)^2. \tag{2}$$

In these equations, θ is the angle between laser polarization and zigzag crystallographic orientation of the flake, and φ is the angle between the uniaxial strain direction and the zigzag direction of MoS₂.

In Eq. (1), the first term corresponds to the phonon mode in the direction of zigzag crystallographic orientation and the second term is corresponding to the phonon mode in the armchair direction. In unstrained or biaxially strained MoS_2 , a = b and c = d which means both degenerate modes of E_{2g}^1 have the same amplitude and overall

 E_{2g}^1 peak amplitude is not a function of measurement angle, θ . The intensity of A_{1g} peak also is not a function of measurement angle θ in unstrained or biaxially strained MoS₂ as Eq. (2) suggests.

Uniaxial strain breaks the symmetry in E^1_{2g} and A_{1g} Raman peaks of MoS₂ and yields a \neq b and c \neq d. ⁴⁰ The A_{1g} has its maximum peak when laser polarization is parallel to strain direction. For the E^1_{2g} peak, under uniaxial strain the two degenerate modes divide into two separate modes. ³⁵ By breaking the degeneracy between the two modes of E^1_{2g} and with a \neq b in Eq. (1), the amplitude of E^1_{2g} becomes a function of θ . Uniaxial tensile strain in an arbitrary direction increases the amplitude of the degenerate mode (zigzag or armchair direction) that is closer to the strain direction. ^{40,41} In this work, the two degenerate modes of E^1_{2g} cannot be evaluated separately since the strain is not large enough to spectrally resolve them into two peaks. ¹⁵ Thus, we must evaluate the E^1_{2g} peak amplitude as a summation of its two modes following the function in Eq. (1).

Figures 4(b)–4(e) present the amplitude of E^1_{2g} and A_{1g} Raman peaks at points A and B as a function of θ , normalized to the amplitude of E^1_{2g} Raman peak of the uncoated part of the same flake at the same measurement angle. As Fig. 4(b) presents, the amplitude of E^1_{2g} at point A shows a four-lobed shape as a function of θ . After fitting the data points of Fig. 4(b) to Eq. (1), we find out that $\varphi=0^\circ$ and a > b, which proves that the strain is parallel to the zigzag direction with 0° difference between the two directions. Similarly, as Fig. 4(c) presents, the amplitude of A_{1g} peaks at point A on the device also varies as a function of θ under uniaxial strain. As it is shown in Fig. 4(c), by fitting the A_{1g} amplitude to Eq. (2), the direction of uniaxial tensile strain can be extracted, which in this case is at $\theta=0^\circ$ presented by arrows at point A in Fig. 4(a).

During mechanical exfoliation, MoS_2 tends to cleave along its zigzag axes (every 60 °), so all free edges are typically of zigzag orientation. Dur results reconfirm this, since according to polarized Raman of E_{2g}^1 and A_{1g} , there is a 0° difference between zigzag direction and strain (which is along $\theta=0^\circ$), thus the zigzag direction is also along $\theta=0^\circ$ and is horizontal in Fig. 4(a).

The same polarized Raman measurements have been conducted at the center of the stressor, and the results are presented in Figs. 4(d) and 4(e). The amplitude of E^1_{2g} and A_{1g} peaks are not a function of θ . As we saw in Fig. 1, the E^1_{2g} peak shifts up at the center of the stressor, which proves the type of strain is biaxial compressive. This type of strain does not break the degeneracy in either MoS₂ Raman peaks.

We have been able to prove that selective strain engineering of 2D MoS₂ is possible by lithographically patterned thin film stressor deposition. The free edges of the tensile stressor produce uniaxial tensile strain in the direction perpendicular to the edge and there is biaxial compressive strain away from the free edges. Therefore, by adjusting the width of such patterned stressors, we can control the in-plane strain distribution within each individual 2D flake. At the same time, we have also demonstrated that we can controllably apply out-of-plane tensile strain to 2D van der Waals bonded materials using this technique, which to our knowledge does not exist by any other mechanism.

By showing these results, we have completely outlined how to translate the full power of process-induced strain engineering from industrial CMOS IC manufacturing to 2D materials. Static strain engineering with the proposed patterned stressors could also be combined with dynamically controlled strain from ferroelectric substrates enabling dynamic control over strain sensitive properties of 2D

materials.^{43,44} Combining all these concepts together with novel strain patterned devices opens the door to a wide variety of unexplored functionalities that can only be achieved at scale by using micropatterned or nanopatterned stressors.

See the supplementary material for more details on the fabrication process, 3D vs 2D strain engineering, flake thickness identification, center strain evolution, Raman power dependence, photoluminescence spectroscopy, and Raman peak intensity maps.

We wish to acknowledge support from the National Science Foundation (Nos. OMA-1936250 and ECCS-1942815) and the National Science Foundation Graduate Research Fellowship Program (No. DGE-1939268). This work also made use of the Cornell Center for Materials Research Shared Facilities, which are supported through the NSF MRSEC program (No. DMR-1719875).

DATA AVAILABILITY

The data that support the findings of this study are available from the corresponding author upon reasonable request.

REFERENCES

- ¹S. E. Thompson, M. Armstrong, C. Auth, M. Alavi, M. Buehler, R. Chau, S. Cea, T. Ghani, G. Glass, T. Hoffman, C. H. Jan, C. Kenyon, J. Klaus, K. Kuhn, Z. Ma, B. Mcintyre, K. Mistry, A. Murthy, B. Obradovic, R. Nagisetty, P. Nguyen, S. Sivakumar, R. Shaheed, L. Shifren, B. Tufts, S. Tyagi, M. Bohr, and Y. El-Mansy, IEEE Trans. Electron Devices 51, 1790 (2004).
- ²J. L. Hoyt, H. M. Nayfeh, S. Eguchi, I. Aberg, G. Xia, T. Drake, E. A. Fitzgerald, and D. A. Antoniadis, in Technical Digest-International Electron Devices Meeting (2002), p. 23.
- ³M. L. Lee, E. A. Fitzgerald, M. T. Bulsara, M. T. Currie, and A. Lochtefeld, J. Appl. Phys. **97**, 011101 (2005).
- ⁴P. R. Chidambaram, C. Bowen, S. Chakravarthi, C. Machala, and R. Wise, IEEE Trans. Electron Devices **53**, 944 (2006).
- ⁵S. B. Desai, G. Seol, J. S. Kang, H. Fang, C. Battaglia, R. Kapadia, J. W. Ager, J. Guo, and A. Javey, Nano Lett. 14, 4592 (2014).
- ⁶S. Manzeli, A. Allain, A. Ghadimi, and A. Kis, Nano Lett. 15, 5330 (2015).
- ⁷H. Guo, N. Lu, L. Wang, X. Wu, and X. C. Zeng, J. Phys. Chem. C 118, 7242 (2014).
- ⁸Y. Liu, Y. Y. Li, S. Rajput, D. Gilks, L. Lari, P. L. Galindo, M. Weinert, V. K. Lazarov, and L. Li, Nat. Phys. **10**, 294 (2014).
- ⁹Y. Bai, L. Zhou, J. Wang, W. Wu, L. J. McGilly, D. Halbertal, C. F. B. Lo, F. Liu, J. Ardelean, P. Rivera, N. R. Finney, X. C. Yang, D. N. Basov, W. Yao, X. Xu, J. Hone, A. N. Pasupathy, and X. Y. Zhu, Nat. Mater. 19, 1068 (2020).
- 10 Y. Wang, C. Cong, W. Yang, J. Shang, N. Peimyoo, Y. Chen, J. Kang, J. Wang, W. Huang, and T. Yu, Nano Res. 8, 2562 (2015).
- ¹¹Y. Ge, W. Wan, F. Yang, and Y. Yao, New J. Phys. 17, 035008 (2015).
- ¹²N. H. Jo, L. L. Wang, P. P. Orth, S. L. Bud'ko, and P. C. Canfield, Proc. Natl. Acad. Sci. 116, 25524 (2019).
- ¹³S. Song, D. H. Keum, S. Cho, D. Perello, Y. Kim, and Y. H. Lee, Nano Lett. 16, 188 (2016).
- ¹⁴C. Si, Z. Sun, and F. Liu, Nanoscale **8**, 3207 (2016).
- ¹⁵H. J. Conley, B. Wang, J. I. Ziegler, R. F. Haglund, S. T. Pantelides, and K. I. Bolotin, Nano Lett. 13, 3626 (2013).

- ¹⁶ A. Castellanos-Gomez, R. Roldán, E. Cappelluti, M. Buscema, F. Guinea, H. S. J. Van Der Zant, and G. A. Steele, Nano Lett. 13, 5361 (2013).
- 17 R. Yang, J. Lee, S. Ghosh, H. Tang, R. M. Sankaran, C. A. Zorman, and P. X. L. Feng, Nano Lett. 17, 4568 (2017).
- ¹⁸J. Quereda, P. San-Jose, V. Parente, L. Vaquero-Garzon, A. J. Molina-Mendoza, N. Agraït, G. Rubio-Bollinger, F. Guinea, R. Roldán, and A. Castellanos-Gomez, Nano Lett. 16, 2931 (2016).
- ¹⁹J. W. Christopher, M. Vutukuru, D. Lloyd, J. S. Bunch, B. B. Goldberg, D. J. Bishop, and A. K. Swan, J. Microelectromech. Syst. 28, 254 (2019).
- ²⁰A. P. Nayak, S. Bhattacharyya, J. Zhu, J. Liu, X. Wu, T. Pandey, C. Jin, A. K. Singh, D. Akinwande, and J. F. Lin, Nat. Commun. 5, 3731 (2014).
- ²¹D. Lloyd, X. Liu, J. W. Christopher, L. Cantley, A. Wadehra, B. L. Kim, B. B. Goldberg, A. K. Swan, and J. S. Bunch, Nano Lett. 16, 5836 (2016).
- ²²A. Reserbat-Plantey, D. Kalita, Z. Han, L. Ferlazzo, S. Autier-Laurent, K. Komatsu, C. Li, R. Weil, A. Ralko, L. Marty, and S. Guéron, Nano Lett. 14, 5044 (2014).
- ²³S. T. Gill, J. H. Hinnefeld, S. Zhu, W. J. Swanson, T. Li, N. Mason, and G. E. T. Al, ACS Nano 9, 5799 (2015).
- ²⁴H. Li, A. W. Contryman, X. Qian, S. M. Ardakani, Y. Gong, X. Wang, J. M. Weisse, C. H. Lee, J. Zhao, P. M. Ajayan, J. Li, H. C. Manoharan, and X. Zheng, Nat. Commun. 6, 7381 (2015).
- ²⁵E. Kim, C. Lee, J. Song, S. Kwon, B. Kim, D. H. Kim, T. J. Park, M. S. Jeong, and D. Kim, J. Phys. Chem. Lett. 11, 3039 (2020).
- ²⁶G. Dushaq, B. Paredes, J. Lu, M. Chiesa, and M. Rasras, ACS Appl. Nano Mater. 3, 10333 (2020).
- ²⁷W.-K. Lee, J. Kang, K.-S. Chen, C. J. Engel, W.-B. Jung, D. Rhee, M. C. Hersam, and T. W. Odom, Nano Lett. 16, 7121 (2016).
- ²⁸T. Peña, S. A. Chowdhury, A. Azizimanesh, A. Sewaket, H. Askari, and S. M. Wu, arXiv:2009.10626 (2021).
- ²⁹M. Yagmurcukardes, C. Bacaksiz, E. Unsal, B. Akbali, R. T. Senger, and H. Sahin, Phys. Rev. B 97, 115427 (2018).
- ⁵⁰C. Rice, R. J. Young, R. Zan, U. Bangert, D. Wolverson, T. Georgiou, R. Jalil, and K. S. Novoselov, Phys. Rev. B 87, 081307 (2013).
- ³¹A. Michail, N. Delikoukos, J. Parthenios, C. Galiotis, and K. Papagelis, Appl. Phys. Lett. 108, 173102 (2016).
- ³²R. Abermann, Vacuum **41**, 1279 (1990).
- ³³N. Kaiser and H. K. Pulker, Optical Interference Coatings (Springer-Verlag, 2013).
- 34H. K. Pulker, Thin Solid Films 58, 371 (1979).
- **35**Y. Wang, C. Cong, C. Qiu, and T. Yu, Small **9**, 2857 (2013).
- ³⁶I. C. Noyan, T. C. Huang, and B. R. York, Crit. Rev. Solid State Mater. Sci. 20, 125 (1995).
- ³⁷I. De Wolf, J. Vanhellemont, A. Romano-Rodríguez, H. Norström, and H. E. Maes, J. Appl. Phys. 71, 898 (1992).
- ³⁸S. C. Jain, A. H. Harker, A. Atkinson, and K. Pinardi, J. Appl. Phys. **78**, 1630 (1995).
- ³⁹I. De Wolf, H. Norström, and H. E. Maes, J. Appl. Phys. 74, 4490 (1993).
- D. Doratotaj, J. R. Simpson, and J. A. Yan, Phys. Rev. B 93, 075401 (2016).
 T. M. G. Mohiuddin, A. Lombardo, R. R. Nair, A. Bonetti, G. Savini, R. Jalil, N. Bonini, D. M. Basko, C. Galiotis, N. Marzari, K. S. Novoselov, A. K. Geim, and
- A. C. Ferrari, Phys. Rev. B 79, 205433 (2009).
 42Y. Guo, C. Liu, Q. Yin, C. Wei, S. Lin, T. B. Ho, Y. Zhao, J. H. Edgar, Q. Chen,
 S. P. Lau, J. Dai, H. Yao, and H. P. Wong, ACS Nano 10, 8980 (2016).
- ⁴³C. Chakraborty, A. Mukherjee, H. Moon, K. Konthasinghe, L. Qiu, W. Hou, T. Peña, C. Watson, S. M. Wu, D. Englund, and N. Vamivakas, Optica 7, 580 (2020)
- ⁴⁴W. Hou, A. Azizimanesh, A. Sewaket, T. Peña, C. Watson, M. Liu, H. Askari, and S. M. Wu, Nat. Nanotechnol. 14, 668 (2019).